photochem

MDPI

Article

Characterizing the Excited States and Electronic Absorption Spectra of Small Alkylperoxy (RO_2•) and Hydroperoxy (•QOOH) Radicals

Lily M. Guidry [1], Sofia E. Guidry [1], Tanima Barua [1], Barbara Marchetti [1], Michael F. Vansco [2,*] and Tolga N. V. Karsili [1,*]

[1] Department of Chemistry, University of Louisiana at Lafayette, Lafayette, LA 70503, USA; lily.guidry1@louisiana.edu (L.M.G.); sofia.guidry1@louisiana.edu (S.E.G.); tanima.barua1@louisiana.edu (T.B.); barbara.marchetti1@louisiana.edu (B.M.)
[2] Department of Chemistry, Coastal Carolina Univeristy, Conway, SC 29528, USA
* Correspondence: mvansco@coastal.edu (M.F.V.); tolga.karsili@louisiana.edu (T.N.V.K.)

Abstract

Organic peroxy (ROO•) and hydroperoxy (•QOOH) radicals are key reactive intermediates that are formed via the oxidation of volatile organic compounds during combustion or in the Earth's atmosphere. Their primary fate is continued unimolecular decay or bimolecular chemistry, the relative branching for which is heavily structure- and temperature-dependent. This article outlines a combined single- and multi-reference quantum chemical study to characterize the near-UV accessible electronically excited states of the prototypical ROO• and •QOOH intermediates, *tert*-butyl peroxy and hydroperoxy-*tert*-butyl radicals—the ground-state chemistries of which have been well studied both experimentally and computationally. Additionally, we simulate the electronic absorption profiles of these ROO• and •QOOH intermediates with a variety of multi- and single-reference methods. The results show an interesting conformer dependence on the electronically excited-state character and electronic absorption maxima of •QOOH. The results show promise for electronic absorption spectroscopy to be used as a selected probe for determining •QOOH conformers. Additionally, electronic absorption may contribute to the daytime removal of long-lived •QOOH intermediates formed in the troposphere. We expect that our studies will motivate experiments on the electronic absorption spectra of experimentally achievable ROO• and •QOOH.

Keywords: peroxy radicals; hydroperoxyalkyl radicals; photo absorption of radicals; excited states

Academic Editor: Wenjing Xiao

Received: 19 August 2025
Revised: 7 September 2025
Accepted: 8 September 2025
Published: 11 September 2025

Citation: Guidry, L.M.; Guidry, S.E.; Barua, T.; Marchetti, B.; Vansco, M.F.; Karsili, T.N.V. Characterizing the Excited States and Electronic Absorption Spectra of Small Alkylperoxy (RO_2•) and Hydroperoxy (•QOOH) Radicals. *Photochem* **2025**, *5*, 26. https://doi.org/10.3390/photochem5030026

1. Introduction

Fuel combustion begins with the oxidation of hydrocarbons (RH) to form reactive hydrocarbon (R•) radicals [1–3]. These R• radicals promptly react with atmospheric O_2, generating alkylperoxy (ROO•) radicals, which typically isomerize via H-atom migration to form hydroperoxyalkyl (•QOOH) radicals [2,3]. This process is summarized in Figure 1.

•QOOH intermediates and their oxidation by O_2 account for the radical chain reactions that maintain autoignition during the combustion process in vehicle engines and are implicated in secondary organic aerosol formation in the atmosphere [4–17]. In the latter, atmospheric •OH radicals initiate the oxidation of volatile RH compounds (Figure 1) emitted into the atmosphere via anthropogenic and biogenic sources. Methane, the most

abundant volatile organic compound in the atmosphere, is removed primarily via oxidation with •OH radicals [18]. Given the abundance of solar radiation in the troposphere, the eventual ROO• and •QOOH radicals may undergo solar photolysis, in competition with their established ground-state unimolecular and bimolecular chemistry [19]. Despite this recognition, the excited-state chemistry of ROO• and •QOOH radicals remains poorly understood. Motivated by this, in this study, we employ high-level multi-reference quantum chemical methods to characterize the electronically excited states and the evolving excited-state chemistry of ROO• and •QOOH compounds. Our model ROO• and •QOOH radicals are, respectively, the *tert*-butyl peroxy and *tert*-butyl hydroperoxyalkyl radicals displayed in Figure 2.

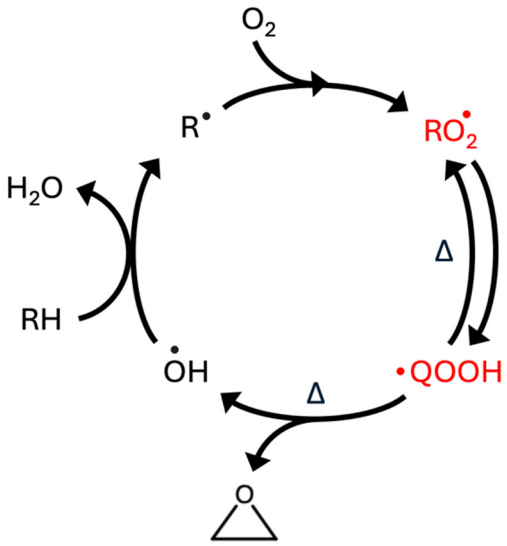

Figure 1. Overview of the oxidation mechanism for forming ROO• and •QOOH, as well as a representative •QOOH unimolecular decay process for regenerating •OH radicals.

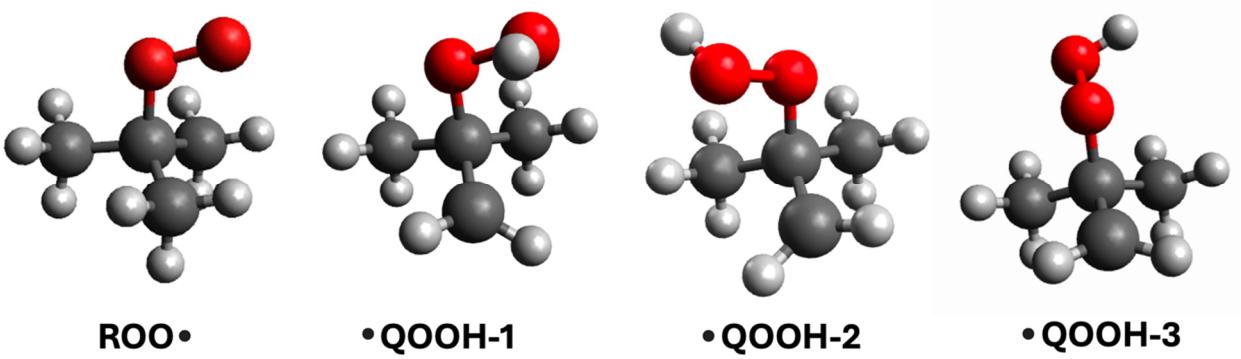

Figure 2. Ground-state minimum energy structures of *tert*-butyl peroxy radical (ROO•) and *tert*-butyl hydroperoxide radical (•QOOH).

The fate of nascent ROO• radicals is temperature-dependent and may undergo bimolecular reactions with bath gases [20–38] or unimolecular decay [3,6,20,39–50]. At atmospheric temperatures, the nascent ROO• radicals typically undergo bimolecular reactions with atmospherically relevant molecules and radicals [20,21,38]. In contrast, combustion-relevant temperatures provide ROO• radicals with sufficient internal energy to undergo unimolecular decay. Under such conditions, the major unimolecular decay path for small ROO• radicals involves HO_2• radical elimination to form stable alkene products [2,3,40–43,45,46,51–59]. For ROO• radicals with four or more carbon atoms, hydrogen-atom migration becomes competitive, with transition state energies that show a

strong dependence on the carbon atom radical site, the structure of ROO•, and the size of the cyclic structure of the transition state [3,39,44,48,52,56,57,60–71]. The resulting •QOOH intermediates are more reactive than their ROO• precursors [2,3,10,64,72–74] and may undergo unimolecular decay to form •OH + epoxide or HO_2 + alkene products, or reform ROO• [2,75–79]. They may also undergo bimolecular reaction with O_2 [2].

There are far fewer studies on electronically excited ROO• radicals, which have been shown to exhibit a strong transition in the ultraviolet region and a substantially weaker transition in the near-infrared region [80–86]. Some studies have explored electronic transitions of ROO• radicals in the ultraviolet region. Neumark and coworkers investigated the photodissociation of *tert*-butyl peroxy radicals at 248 nm using fast-radical-beam coincidence translational spectroscopy [87]. They found the major channel to be three-body fragmentation to O, CH_3, and acetone, and minor two-body fragmentation channels leading to the formation of O_2 + *tert*-butyl radical and HO_2 + isobutene. McGivern and co-workers have undertaken photochemical studies on heavy (C_{12}) ROO• radicals [12,19]. Following irradiation at 254 nm, the resulting electronically excited ROO• radical primarily undergoes intramolecular rearrangement to form •QOOH radicals, as well as unimolecular decay to form R• + O_2 and alkene + HO_2 products. The large absorption cross sections of ROO• radicals in the region that overlaps with the solar actinic flux indicate solar photolysis may be competitive with bimolecular reactions in the atmosphere [19].

Other studies have explored the electronic spectroscopy of ROO• radicals in the near-infrared region. Fittschen et al. [83] and Miller et al. [85] have reported the absolute absorption cross section of the first electronic transition of the ethyl peroxy radical. An earlier report by Vaida et al. [82] suggested that photolysis of ROO• radicals via their first electronic transition could compete with rates for bimolecular reactions with NO and HO_2, depending on the magnitude of the absorption cross section. The small absorption cross section measured for the ethyl peroxy radical (ca. 0.5–1.0 $\times$ 10^{-20} cm^2) aligns with the lower limit used by Vaida et al. in estimating photolysis rates of simple ROO• radicals. Assuming other ROO• radicals have similar absorption cross sections for their first electronic transition suggests photolysis will play a small, but non-negligible role in the removal of ROO• from the atmosphere. Furthermore, Schaefer and co-workers have modeled the ground and first electronically excited states of the methyl peroxy and *tert*-butyl peroxy radicals, with the aim of systematically refining their spectroscopic predictions [88,89].

In this article, we use single- and multi-reference quantum chemical methods to characterize the electronically excited states of *tert*-butyl peroxy (henceforth ROO) and *tert*-butyl hydroperoxyalkyl (henceforth QOOH) radicals and simulate their electronic absorption spectra. We benchmark various methods of Time-Dependent Density Functional Theory (TDDFT) to enable a future modeling study of the excited-state dynamics and spectroscopy of ROO and QOOH radicals with increasing molecular complexity. Given that the ROO and QOOH radicals studied in this article have previously been prepared in vacuum experiments, our results should inform experimentalists on appropriate wavelength regions to probe these transient reactive intermediates and enable future photochemical experiments that may be of atmospheric relevance.

2. Methodology

The ground-state minimum energy geometry of ROO and QOOH was optimized using the B2PLYPD3 functional of Density Functional Theory (DFT), coupled to Dunning's correlation consistent basis set of triple-ζ quality: cc-pVTZ. Normal mode analysis was conducted to ensure that all optimized structures were minima. This functional and basis set combination has been shown to perform well in providing accurate structures and normal mode wavenumbers for various reactive intermediates, including QOOH

intermediates [77–79,90–94]. Various rotational isomers of QOOH were also optimized and scans connecting these various minima were computed by means of a linear interpolation in internal coordinates at the explicitly correlated CCSD(T)-F12/cc-pVTZ-F12 level of theory.

Vertical excitation energies and oscillator strengths for ROO and three isomers of QOOH were computed on the optimized structures through TDDFT, using a variety of density functionals and basis sets. To benchmark the TDDFT vertical excitation energies, additional vertical excitation energies were computed using complete active space second-order theory (CASPT2), utilizing an active space of nine electrons arranged in seven orbitals (9/7), and a state-averaged complete active space self-consistent field (SA-CASSCF) reference wavefunction. The lowest three states of doublet spin-symmetry were used in all SA-CASSCF calculations. The active space orbitals are depicted in Figure S1.1–S1.4 of the Supporting Information. Our active space was guided by the initial valence electrons of the R + O_2 reactants, coupled with a need to describe all relevant electronic effects of the ROO and QOOH intermediates while maintaining a reasonable computational cost. An imaginary level shift of 0.4 E_H was used to aid convergence and mitigate the involvement of intruder states. We note that other single-reference methods such as CC2 and ADC(2) would also be appropriate for the present ROO and QOOH intermediates and provide additional benchmarks, but these would become restrictive in our future studies on larger and more complex ROO and QOOH intermediates.

Electronic absorption spectra were then simulated for ROO and three relevant conformers of QOOH. A thermal distribution of ground-state geometries was obtained using ab initio molecular dynamics (AIMD) for each of the ROO and QOOH structures. In AIMD, the time evolution of the nuclear coordinates is determined by numerically integrating Newton's equations, while at each time step, the energies and forces are computed explicitly using electronic structure theory. First, the optimized ROO and QOOH structures were equilibrated in the NVT ensemble (with T = 298 K) for 10 picoseconds. This temperature was chosen to mimic the conditions of potential laboratory experiments under thermal conditions. The subsequent equilibrated structure was propagated for a further 10 picoseconds in the same NVT ensemble, with a step size of 1 fs. From the second simulation, 500 structures (every 10 fs) were extracted, and vertical excitation energies were computed at the same CASPT2 level of theory as described above, as well as the best level of DFT identified in the benchmark computations. The excitation energy dependent photoabsorption cross section $\sigma(E)$ was then obtained using Equation (1),

$$\sigma(E) = \frac{\pi e^2}{2m_e c\varepsilon_0} \sum_{j=1}^{M} \left[\frac{1}{N_{TOT}} \sum_{N=1}^{N_{TOT}} f_{ij}^N g\left(E - \Delta E_{ij}^N,\, \delta\right) \right] \tag{1}$$

where g is a Lorentzian line shape function given by Equation (2),

$$g\left(E - \Delta E_{ij}^N,\, \delta\right) = \frac{\hbar\delta}{2\pi} \left(\left(E - \Delta E_{ij}^N\right)^2 + \left(\frac{\delta}{2}\right)^2 \right)^{-1} \tag{2}$$

f_{ij} is the oscillator strength given by Equation (3),

$$f_{ij}^N = \frac{2}{3} \left(\Delta E_{ij}^N\right) \sum_{\alpha=x,y,z} \left| \mu_{ij}^N \right|_\alpha^2 \tag{3}$$

and $\Delta E_{ij}^N = \left(E_j^N - E_i^N\right)$, m_e and e are the mass and charge of the electron, respectively, while c is the speed of light. The internal sum in Equation (1) is expressed over the set of total geometries (N_{TOT} = 500) while the external sum includes transitions from the initial state i (the ground state) to final state j (i.e., S_1, S_2, S_3, …, S_M etc.) with respective oscillator

strength f_{ij}^{N} as given by Equation (3). δ is a broadening factor, which is arbitrarily set to 0.2 eV for each of the calculated absorption profiles reported herein. All CASPT2 and CCSD(T) calculations were performed in Molpro [95,96], while the DFT computations were undertaken in Gaussian 16 [97].

3. Results and Discussion

Figure 2 presents the molecular structure associated with the ground-state minimum energy geometry of ROO. As expected, the minimum energy geometry shows a staggered conformation of the terminal oxygen relative to the methyl substituents. This conformation is reminiscent of the expected stereochemistry of alkanes in which the staggered configuration is favored. This geometry is reinforced by Figure 3, which presents the potential energy (PE) profiles connecting the equivalent staggered conformations of ROO as illustrated by the associated Newman projections at the minima. As evident in this figure, rotation about the C-O bond (f_{CCOO}), connecting two equivalent staggered conformations, traverses a geometry in which the terminal oxygen eclipses a methyl substituent. As is well known and confirmed by Figure 3, the eclipsed conformation is a saddle point along the PE surface. The PE barrier along nuclear motions corresponding to staggered-to-eclipsed transformation is ~3.15 kcal mol^{-1}, precluding free rotation around the C-O bond at tropospherically relevant temperatures (~220–290 K) and minimal free rotation at low-temperature combustion temperatures (500–700 K).

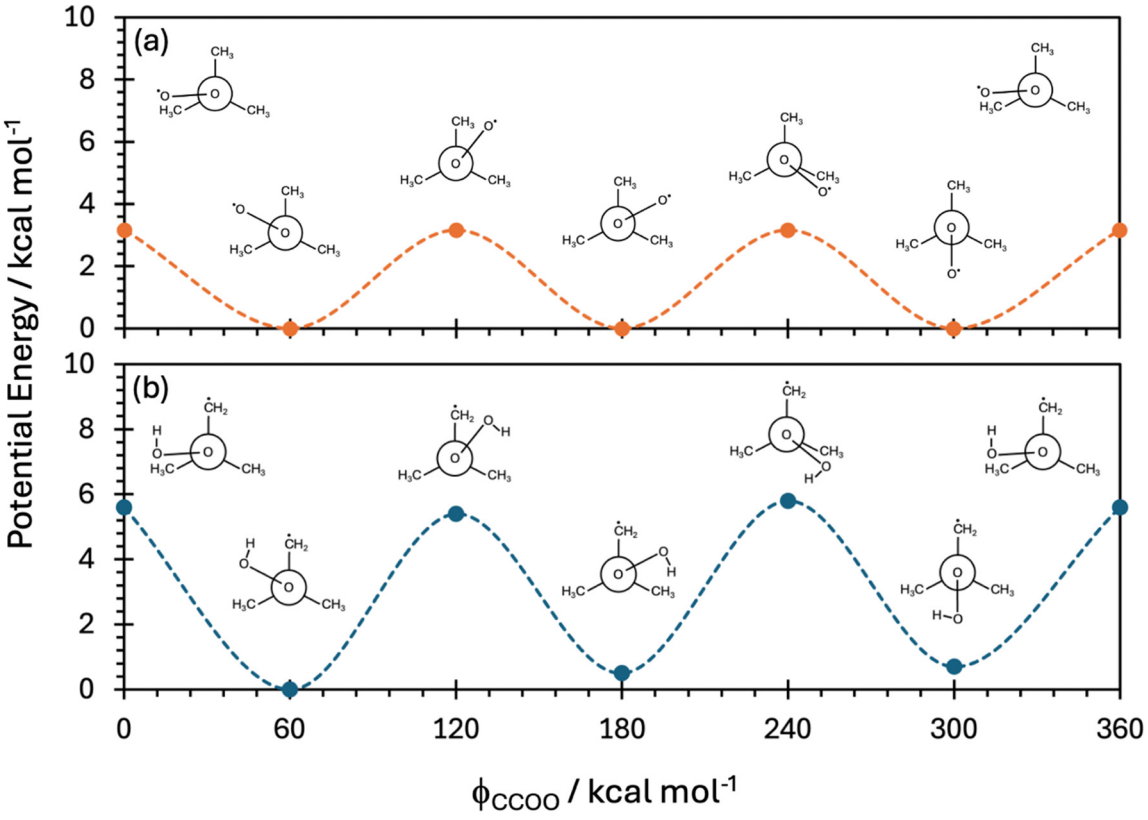

Figure 3. Potential energy (PE) profiles connecting the various minimum energy conformations and transition state structure connecting the relevant conformers of (**a**) ROO calculated at the CCSD(T)-F12b/cc-pVTZ-F12 level and (**b**) QOOH calculated at the same level of theory. Newman projections of the various conformers are displayed alongside the relevant points along the PE profile. The filled data points are optimized minimum energy and transition state structures while the dashed line is a spline through the data points.

As noted in the introduction, intramolecular hydrogen-atom migration from an alkyl group adjacent to the terminal oxygen is a competitive unimolecular decay route for ROO in low-temperature combustion conditions as well as for a subset of atmospherically relevant peroxy radicals—particularly those derived from the atmospheric oxidation of isoprene. In our prototypical ROO, the *tert*-butyl peroxy radical, 1,4-hydrogen migration forms a 2-hydroperoxy-2-methylprop-1-yl (QOOH) radical, inevitably shifting the singly occupied molecular orbital (SOMO) that carries the unpaired electron (see Figure 4). Unlike ROO, the inherent asymmetry of the nascent QOOH leads to three distinct staggered conformations, as illustrated in Figure 2. The relevant conformer formed following hydrogen-atom migration is QOOH-1, as it is the lowest energy staggered conformation. The latter is seen clearly in Figure 3b, which presents the PE profiles associated with the f_{CCOO} coordinate of QOOH—the coordinate that connects the three distinct staggered conformations. As evident from these PE profiles, the QOOH-2 and QOOH-3 conformers are, respectively, ~0.5 kcal mol^{-1} and ~0.7 kcal mol^{-1} less stable than QOOH-1, consistent with the results of Hansen et al. [76]. The relative stability can be understood by recognizing the loss of hydrogen-bonding found in QOOH-1 between the terminal H-atom of the hydroperoxy group and the SOMO lone electron.

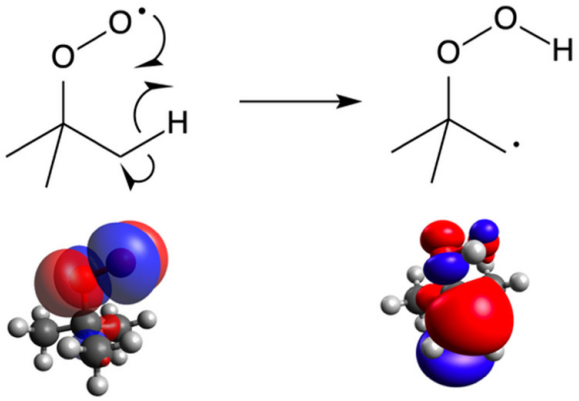

Figure 4. Molecular structure and singly occupied molecular orbital (SOMO) of the ROO and QOOH radicals.

We now turn our attention to the excited-state characteristics of ROO and the three QOOH radicals. Such an analysis first warrants a brief discussion on the ground-state electronic structure of these radicals. The valence electronic structure of ROO and QOOH is depicted through the schematic molecular orbital diagram in Figure 5. As illustrated in Figure 5, the valence electronic structure of ROO can be understood by combining the valence orbitals of O_2 with the *tert*-butyl radical. The ground state of O_2 is of $^3\Sigma_g^+$ character—manifesting from an orthogonal and degenerate pair of singly occupied π^* orbitals. Formation of ROO occurs when an unpaired electron in one of these π^* orbitals interacts with the unpaired electron in the singly occupied 2p orbital of the *tert*-butyl radical. The overlap of the 2p and π^* orbitals, respectively, of the *tert*-butyl radical and the O_2 molecule leads to a new pair of σ_{CO} and σ_{CO}^* ($p_y\pi_y^*$ and $[p_y\pi_y^*]^*$ in Figure 5, respectively) molecular orbitals in the resulting ROO orbitals. Given that the pre-existing π_{OO}^* (π_y^* in Figure 5) orbital is now doubly occupied, the corresponding π electrons transform into an O-centered lone pair (labeled p_y in Figure 5). The remaining π_{OO}^* orbital in the resulting ROO radical is the SOMO (labeled π_x in Figure 5).

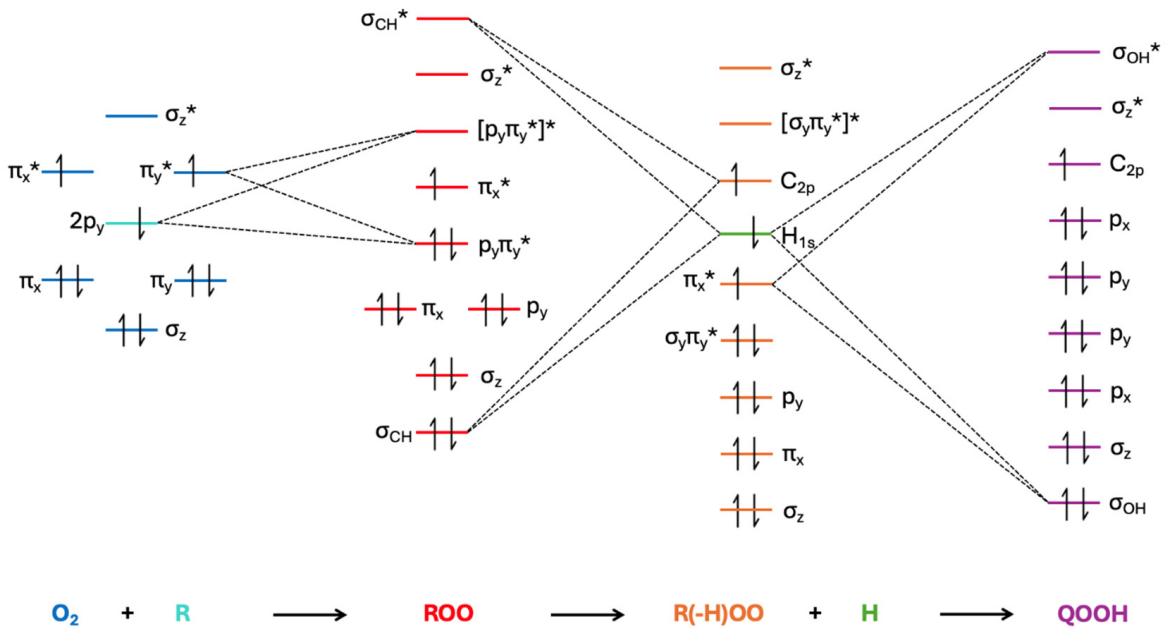

Figure 5. Schematic of the change in molecular orbitals upon the R + O_2 reaction to form ROO, as well as its subsequent rearrangement to form QOOH.

The hydrogen-atom migration that leads to the transformation of ROO to QOOH involves C-H bond cleavage, followed by formation of an O-H bond. The change in electronic structure upon ROO to QOOH transformation is described in Figure 5—wherein homolytic bond fission of a methyl-centered C-H bond leads to a dehydrogenated ROO (henceforth R(-H)OO) + H combination with singly occupied H 1s and C 2p orbitals, isoenergetic with the valence orbitals of R(-H)OO. Formation of QOOH occurs via the interaction of the H 1s electron and the unpaired electron in the p_x* orbital, leading to a s_{OH} and s_{OH}* pair and a non-bonding electron in the C 2p orbital, which transforms to SOMO. Given the pairing of the second unpaired p_x* electron, the O-O bond order decreases to 1, thus transforming the pre-existing p electrons into oxygen-centered lone pairs.

Figure 6 illustrates the relevant molecular orbitals involved in the highest three contributing electronic configurations ($\Psi_1(D_0)$, $\Psi_2(D_0)$, $\Psi_3(D_0)$) to the ground state (D_0) of ROO. When compared to Figure 5, these three relevant orbitals are equivalent to the π_x, π_x* and σ_{CH} orbitals and are thus labeled as such in Figure 6; π_x* is the SOMO. As Figure 6 shows, D_0 is dominantly of Ψ_1 electronic character with a very minor (3%) contribution from Ψ_3. Although 91% Ψ_1 character includes some multi-reference character, a 91% contribution from Ψ_1 indicates that ROO radicals may be adequately represented by high-level single-reference electronic structure methods. The D_1 and D_2 states of ROO are primarily of, respectively, Ψ_2 and Ψ_3 configurations, and are formed via, respectively, $\pi_x^* \leftarrow p_y\pi_y^*$ and $\pi_x^* \leftarrow \pi_x$ excitations. As Table 1 shows, the $D_1 \leftarrow D_0$ transition is predicted to absorb at near-IR wavelengths but with zero absorption cross section, as implied by the predicted zero oscillator strength. The latter manifests from the poor spatial overlap between the π_x* and $p_y\pi_y$* orbitals involved in preparing the D_1 state. In contrast, the $D_2 \leftarrow D_0$ transition is expected to strongly absorb at mid-UV wavelengths. The accompanying high oscillator strength is a manifestation of the favorable spatial overlap between the parallel π_x and π_x* orbitals.

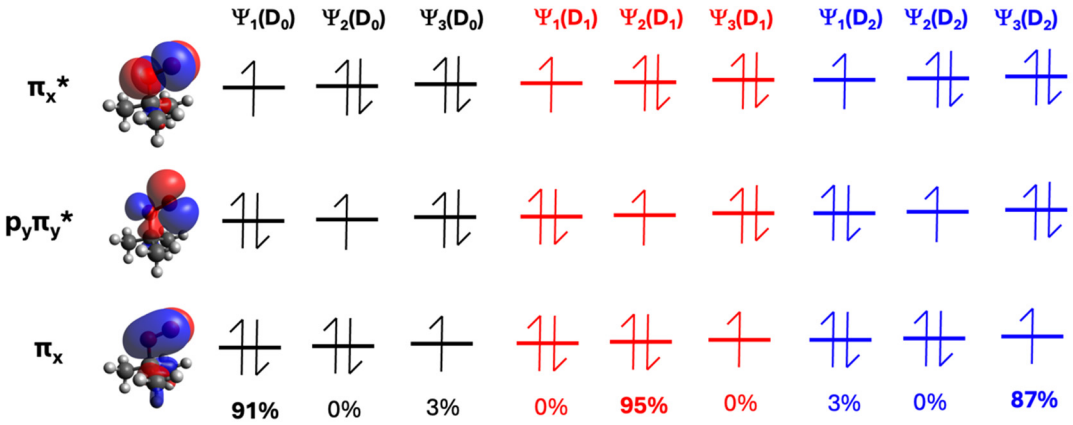

Figure 6. Orbitals and orbital promotions associated with ROO.

Table 1. Vertical excitation energies (VEEs) and oscillator strengths associated with the $D_1 \leftarrow D_0$ and $D_2 \leftarrow D_0$ transitions of ROO and three relevant conformers of QOOH. These are computed at the CASPT2/aug-cc-pVTZ level of theory.

Species	$D_1 \leftarrow D_0$ Transition		$D_2 \leftarrow D_0$ Transition	
	VEE	Oscillator Strength	VEE	Oscillator Strength
ROO 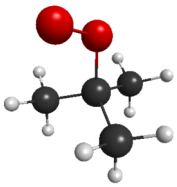	1.20 eV (1033.2 nm)	0.0000	5.70 eV (217.5 nm)	0.5259
QOOH (conformer 1) 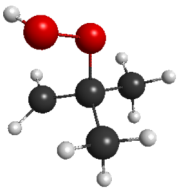	4.55 eV (290 nm)	0.0183	5.37 (234 nm)	0.0110
QOOH (conformer 2) 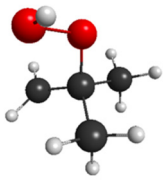	4.63 eV (268 nm)	0.0000	5.72 eV (217 nm)	0.0008
QOOH (conformer 3) 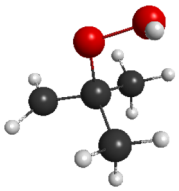	3.52 eV (352 nm)	0.0003	4.55 eV (272 nm)	0.0001

The excited-state characters of the QOOH conformers are less clear cut. Table 1 lists the vertical excitation energies and oscillator strengths of the lowest three conformers of QOOH (labeled QOOH-1, QOOH-2, and QOOH-3 from most to least stable). The $D_1 \leftarrow D_0$ and $D_2 \leftarrow D_0$ electronic transitions are predicted to occur upon absorption of near- and mid-UV wavelengths, respectively. For the global minimum energy conformer, QOOH-1, both $D_1 \leftarrow D_0$ and $D_2 \leftarrow D_0$ electronic transitions are predicted to contain appreciable oscillator strength, while QOOH-2 and QOOH-3 are predicted to contain comparatively weaker oscillator strengths. Understanding these latter changes in conformer-dependent absorption cross section requires close analysis of the orbitals involved in the $D_1 \leftarrow D_0$ and $D_2 \leftarrow D_0$ electronic transitions. Starting with the most stable QOOH-1 conformer, Figures 7–9 present the relevant orbitals and orbital occupancies associated with the highest three contributors to the electronic configurations of the D_0 and D_1 states of the QOOH conformers. Again, these orbitals are labeled according to their equivalents in Figure 5. As with ROO, the three most probable electronic configurations of QOOH-1 are the same for both the D_0 and D_1 states, with the domineering electronic configuration predicted to be Y_1 for the D_0 state. In contrast to ROO, the D_1 state of QOOH-1 involves a mixture of Y_2 and Y_3 configurations, both of which involve electron promotion from an oxygen-centered lone-pair (p_x or p_y) to SOMO. This mixed configuration can be understood by recognizing that p_x and p_y are a near-degenerate set of orthogonal lone pairs centered on the oxygen atoms—analogous to those in water and hydrogen peroxide. Given the similarity in the starting orbital, the $D_1 \leftarrow D_0$ and $D_2 \leftarrow D_0$ transitions are accompanied by appreciable oscillator strength.

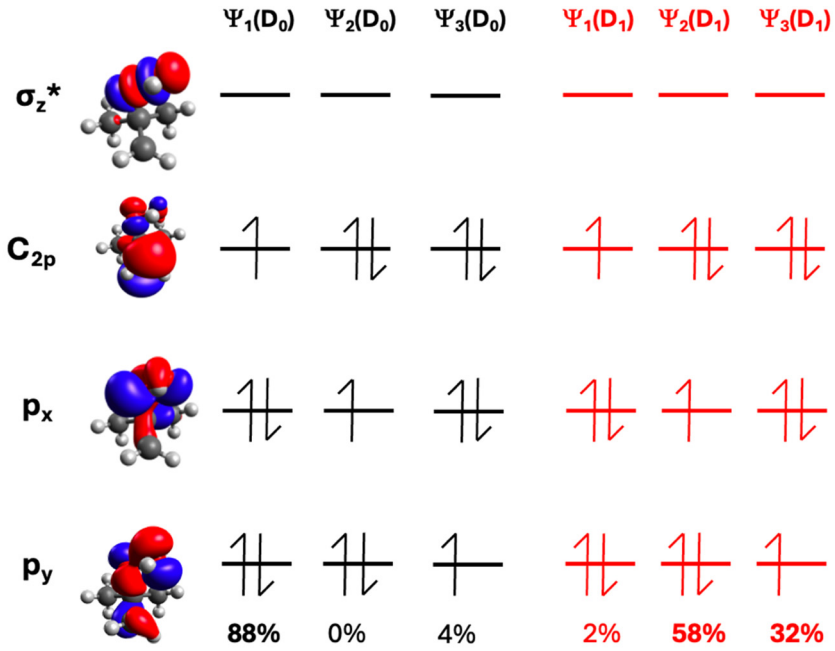

Figure 7. Electronic structure contributions to the D_0 (black) and D_1 (red) states of QOOH-1.

Figure 8 illustrates the highest four contributing electronic configurations of the D_0 and D_1 states of QOOH-2. As with QOOH-1, the D_0 state involves an electronic configuration that is ~90% Ψ_1—with minor contributions from Ψ_2 and Ψ_3 configurations. Unlike QOOH-1, a new electronic configuration—Ψ_4—has a minor contribution to the electronic structure of ground-state QOOH-2. Although a minor component, an increased % contribution of the Ψ_4 configuration may be understood by visualizing the SOMO and LUMO of QOOH-1 (Figure 7) and QOOH-2 (Figure 8) and recognizing that while the electron density distribution of the SOMO and LUMO is primarily localized around the 2p and σ^*_{OO} orbitals,

respectively, they each contain a minor component attributable to the orbital character of its partner pair. This implies that upon QOOH-1 to QOOH-2 transformation, the SOMO and LUMO orbitals couple, which is plausibly explained by the smaller energy difference between SOMO and LUMO (0.46 E_H for QOOH-1 and 0.21 E_H for QOOH-2) and thus an increased contribution from electronic configurations that involve electron promotions to LUMO.

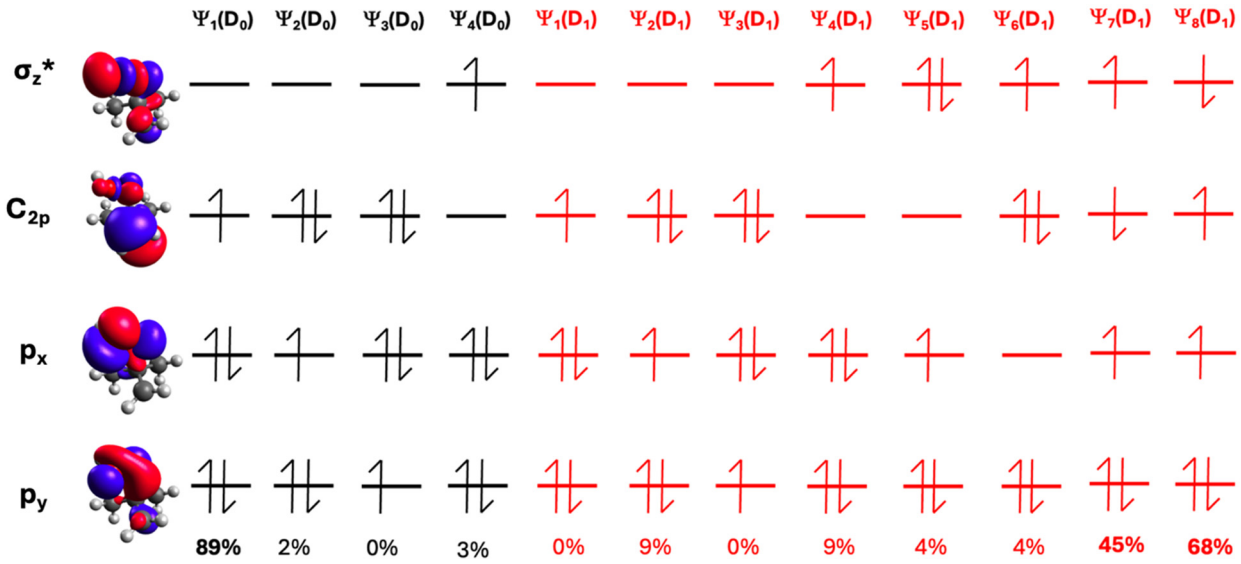

Figure 8. Electronic structure contributions to the D_0 (black) and D_1 (red) states of QOOH-2.

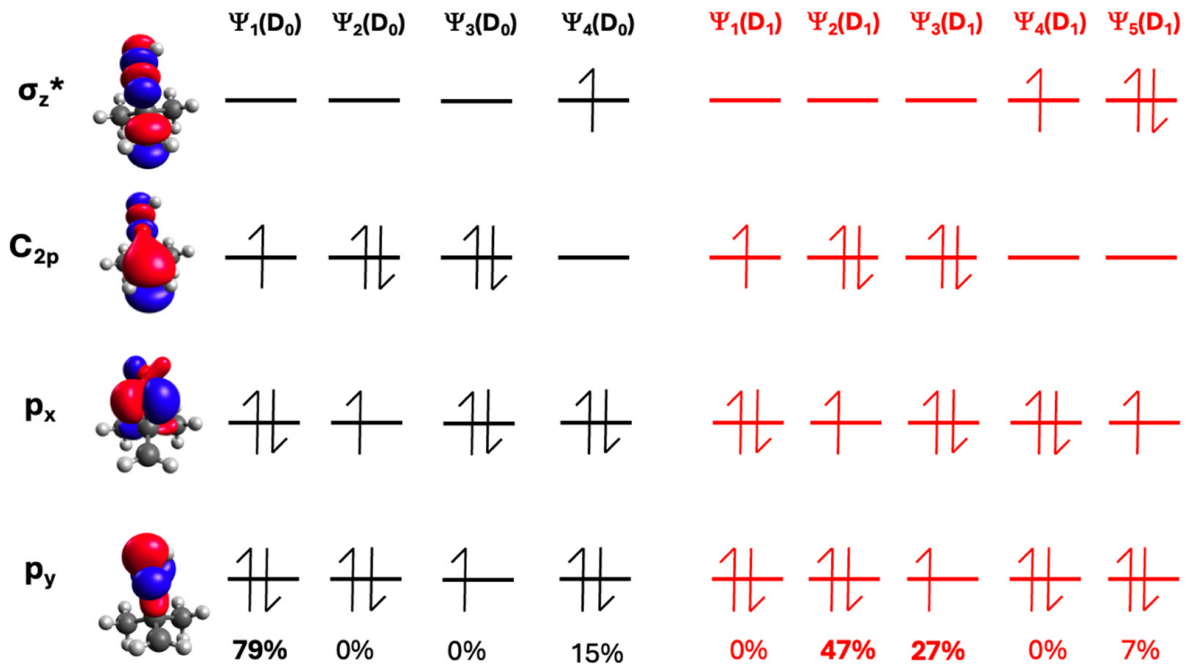

Figure 9. Electronic structure contributions to the D_0 (black) and D_1 (red) states of QOOH-3.

The D_1 state of QOOH-2 is a complicated mixture of several electronic configurations, with the Ψ_7 and Ψ_8 configurations identified as the largest contributors. These configurations are doubly degenerate equivalents, distinguishable by the spin symmetry of the odd electron in the SOMO and LUMO. This observation aligns with near equal contribution of the Ψ_7 and Ψ_8 configurations. Formation of the Ψ_7 and Ψ_8 electron arrangements most likely involve a HOMO to LUMO transition from the Ψ_1 configuration—manifesting in

a 2p ← n transition. Given that the participating orbitals in the dominant transition are orthogonal, their poor spatial overlap manifests in zero oscillator strength for the $D_1 \leftarrow D_0$ transition given in Table 1.

The highest energy QOOH-3 conformer is the relevant conformer implicated in the thermal unimolecular decay of QOOH intermediates to form the chain propagating OH + epoxide products. In contrast to QOOH-1 and QOOH-2, the ground state of QOOH-3 is highly multi-reference, as reflected by the significant reduction in the contribution of the Ψ_1 configuration and an enhanced contribution from the Ψ_4 configuration (see Figure 9). The enhancement of the Ψ_4 electronic configuration can be understood by considering the greater coupling between the SOMO and LUMO and the favorable orientation for an eventual intramolecular S_N2 reaction to leads to OH elimination and epoxide formation.

The D_1 state of QOOH-3 can be described as a mixture of three electronic configurations, $\Psi_2(D_1)$, $\Psi_3(D_1)$, and $\Psi_5(D_1)$—with the former two dominating the D_1 state character. Upon $D_1 \leftarrow D_0$ transition, the $\Psi_2(D_1)$ configuration is formed via a SOMO ← HOMO electron promotion, while the $\Psi_3(D_1)$ configuration is formed via a SOMO ← HOMO-1 electron promotion. The minor $\Psi_5(D_1)$ configuration may be formed via LUMO ← HOMO electron promotion from the $\Psi_4(D_0)$ parent configuration. The small but non-negligible oscillator strength that accompanies the $D_1 \leftarrow D_0$ transition is a manifestation of the low spatial overlap between the participating orbitals in the three electron promotion combinations identified above, i.e., SOMO ← HOMO, SOMO ← HOMO-1, and LUMO ← HOMO, which are orthogonal in all cases. It is particularly noteworthy that while the absorption cross section of QOOH-3 is smaller than QOOH-1, the peak absorption maximum (λ = 352 nm) and thus the long wavelength onset is predicted to align better with the tropospherically relevant solar irradiance.

Having described the vertical excitation energies of the three QOOH conformers and their striking variations upon rotational isomerization, we now turn our attention to presenting the expected electronic absorption profiles of ROO, QOOH-1, QOOH-2, and QOOH-3. Our prior simulations of the electronic absorption spectra of Criegee intermediates [98–101] involved a Wigner distribution of starting structures and subsequent computation of the vertical excitation energies and oscillator strengths. Although the electronic absorption profile was in excellent agreement with the experimentally measured spectra, recent studies have shown that Wigner distribution is unsuitable for low-frequency motions such as methyl rotational motions, which are found in our present study [102]. We have therefore elected to sample the thermal distribution of ground-state geometries using ab initio molecular dynamics. The resulting geometries are used to compute VEEs and oscillator strengths at the CASPT2 level of theory, from which the blue electronic absorption profiles in Figure 10 for ROO and the three conformers of QOOH are derived.

Given the inherent computational cost of the non-black-box CASPT2 level of theory, we computed additional VEEs and oscillator strengths at the TDDFT level of theory to assess the agreement between single- and multi-reference quantum chemical methods and thus the potential for extending the present studies to ROO/QOOH radicals with increased molecular complexity. Table 2 lists the VEEs and oscillator strengths computed with various DFT functional/basis set combinations, alongside the CASPT2 benchmark. For ROO, Table 2 indicates that VEEs calculated with the LC-BLYP functional show the best agreement with CASPT2, alongside a small but noticeable variation with changes in the basis set. While the smallest basis set, 6-31G(d), shows the best agreement, this observation is most likely due to fortuitous cancelation of errors that are inherent to DFT-derived energies. One key observation from Table 2 is that the inclusion of long-range correlation shows an overall better agreement with CASPT2. While the BLYP pure functional shows the best agreement with CASPT2, the PBE pure functional shows poor performance, which

may plausibly manifest from its inability to sufficiently model organic molecules. Given the good performance of LC-BLYP, the electronic absorption spectrum for ROO was simulated using VEEs computed with this functional—the resulting spectra for which are depicted in orange in Figure 10a. As evident from this figure, the agreement between the CASPT2- and LC-BLYP-derived electronic absorption profiles is excellent.

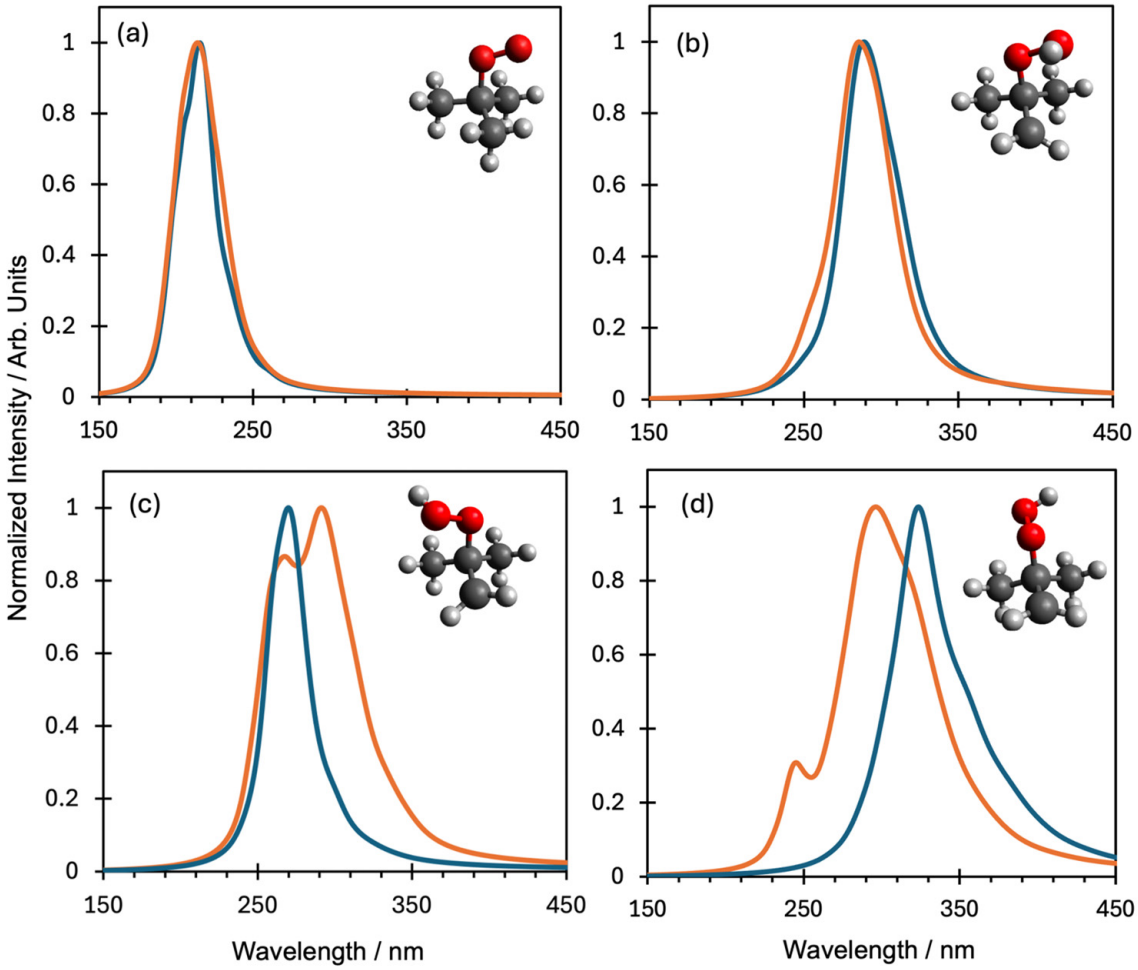

Figure 10. Simulated electronic absorption spectra for (**a**) ROO and (**b**–**d**) the three conformers of QOOH computed at the CASPT2 (blue) and TDDFT (orange) levels of theory.

Analogous benchmark studies were undertaken on the three QOOH conformers. Table 2, alongside Figure 11, lists and pictorially illustrates the VEEs of the various DFT functional/basis set combinations and their deviations from the benchmark CASPT2 level. Inspecting both Table 2 and Figure 11, the performance of the TDDFT-derived VEEs is heavily conformer-dependent. For QOOH-1, VEEs calculated with functionals corrected for long-range correlation (e.g., CAM-B3LYP, ωB97XD, etc.) appear to provide better agreements with the CASPT2-derived VEE, although LC-BLYP shows an over-estimation of the VEE. This latter observation indicates the importance of including Hartree–Fock exchange in the components of the functional. Computing the VEEs using CAM-B3LYP on the equivalent AIMD-derived structures yields the orange electronic absorption profile displayed in Figure 10b, which shows excellent agreement with the CASPT2 electronic absorption profile. Conversely, the CAM-B3LYP electronic absorption profiles for QOOH-2 and QOOH-3 (Figure 10c,d, respectively) are in noticeably poorer agreement with the CASPT2-derived profile. Upon inspecting Table 2 and Figure 11, all DFT functionals underestimate the VEE (cf. CASPT2), except for LC-BLYP. In contrast, all DFT functionals

overestimate the VEE (cf. CASPT2), except for the PBE- and B3LYP-based functionals. Interestingly, as Figures 7–9 indicate, there is a progressive increase in the multi-reference character of the ground state. Moreover, the D_1 state of QOOH-2 involves a significant mixing of electronic configurations that corresponds to doubly excited configurations (Ψ_7 and Ψ_8), when viewed from the dominant ground-state configuration Ψ_1. Given the inherent inability of linear-response DFT to describe double excitations, it is unsurprising that the electronic absorption profiles and VEE are in poor agreement with CASPT2. We also note that the TDDFT simulated absorption profile of QOOH-2 (and to a lesser extent, QOOH-3) is bimodal, which arises via the inability of adiabatic TDDFT to describe double excitations. As illustrated in Figure 8, the leading electronic configurations involve double excitations while the highest single excitation contributions are from configurations Ψ_2 and Ψ_4—both of which contribute 9%. The bimodal character in QOOH-2 is a manifestation of the interplay between these single excitations with subtle changes in geometry in the AIMD ensemble. Future studies will involve modified TDDFT methods, such as spin-flip TDDFT, to describe double excitations.

Table 2. Benchmark calculations of vertical excitation energies (DE) computed at various TDDFT levels of theory and their energetic difference relative to CASPT2 (d). The energies are reported in eV.

Level of Theory	**ROO**		**QOOH-1**		**QOOH-2**		**QOOH-3**	
	Δ*E*	***δ***	**Δ*E***	***δ***	**Δ*E***	***δ***	**Δ*E***	***δ***
CASPT2/AVTZ	5.70	-	4.55	-	4.63	-	3.52	-
CAM-B3LYP/6-311+G(d,p)	5.30	0.40	4.51	0.04	4.51	0.12	3.93	0.42
CAM-B3LYP/6-31+G(d)	5.31	0.39	4.56	0.01	4.54	0.09	3.95	0.44
CAM-B3LYP/AVDZ	5.28	0.42	4.50	0.05	4.50	0.12	3.91	0.39
CAM-B3LYP/VDZ	5.52	0.18	4.48	0.07	4.54	0.08	3.92	0.40
ωB97xD/6-311+G(d,p)	5.27	0.43	4.38	0.17	4.52	0.11	3.89	0.37
ωB97xD/6-31+G(d)	5.28	0.42	4.44	0.11	4.57	0.06	3.92	0.40
ωB97xD/AVDZ	5.26	0.44	4.37	0.18	4.50	0.13	3.87	0.35
ωB97xD/VDZ	5.47	0.23	4.35	0.20	4.49	0.14	3.86	0.35
B3LYP/6-311+G(d,p)	5.04	0.66	3.91	0.64	4.04	0.59	3.42	0.10
B3LYP/6-31+G(d)	5.05	0.65	3.96	0.59	4.08	0.54	3.45	0.07
B3LYP/AVDZ	5.03	0.67	3.90	0.65	4.00	0.63	3.39	0.13
PBE/6-311+G(d,p)	4.31	1.39	3.01	1.54	3.01	1.69	2.43	1.09
PBE0/6-311+G(d,p)	5.15	0.55	4.24	0.31	4.35	1.61	3.70	0.18
LC-BLYP/6-31G(d)	5.69	0.01	5.10	0.55	4.67	0.28	4.41	0.89
LC-BLYP/6-31+G(d)	5.50	0.20	5.02	0.47	4.68	0.04	4.33	0.82
LC-BLYP/6-311+G(d,p)	5.49	0.21	4.99	0.44	4.77	0.06	4.32	0.80

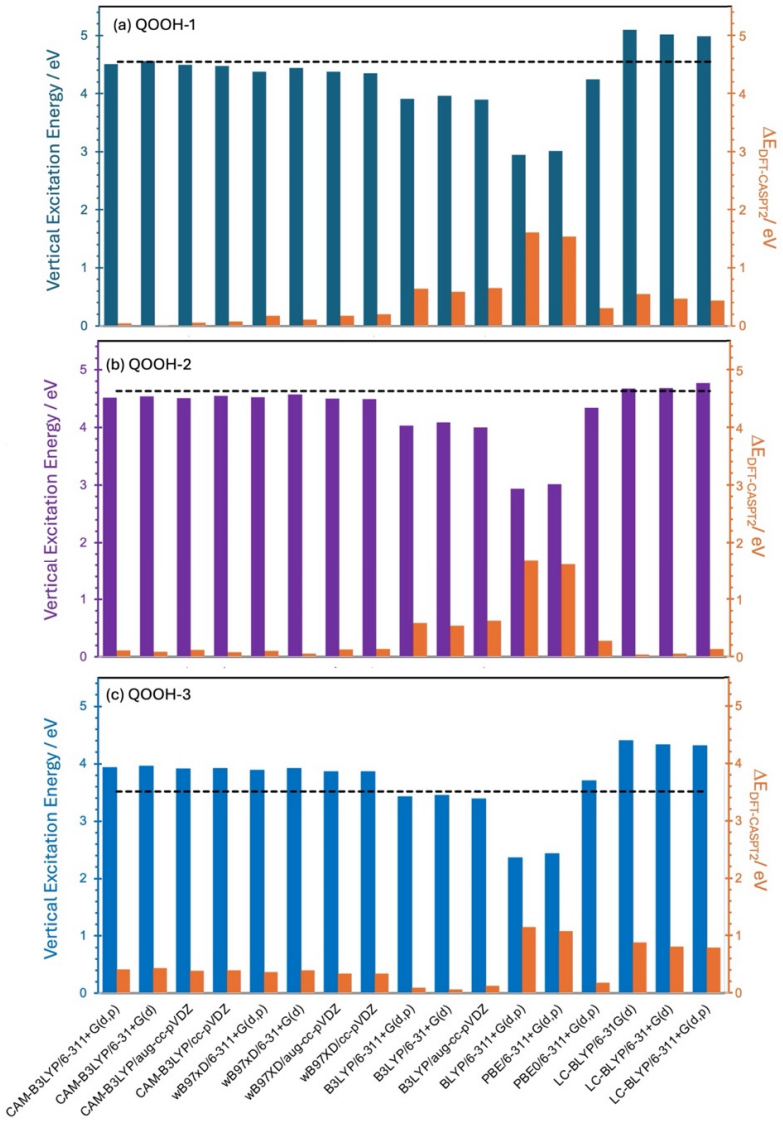

Figure 11. Benchmark vertical excitation energies of various DFT functional/basis set combinations and their energetic difference (orange bars) to that determined with CASPT2 (black dashed line).

4. Conclusions

In the present article, we have undertaken a robust quantum chemical study to characterize the excited states of the simplest ROO and QOOH intermediates—*tert*-butyl-peroxy and *tert*-butyl-hydroperoxy radicals, respectively. These specific ROO and QOOH radicals were chosen due to their experimental convenience, as they have been previously generated in jet-cooled vacuum experiments. Such vacuum experiments may be extended to those that probe excited-state dynamics (specifically, velocity map imaging—VMI). The Lester group have successfully generated the *tert*-butyl-hydroperoxy QOOH radical and undertaken energy-dependent kinetic studies [76,103]. Such experimentation could be trivially extended to VMI experiments as demonstrated in their past studies on Criegee intermediates [100,101,104–108]. Our present study is intended to motivate such experimental studies, specifically using electronic absorption spectroscopy as a probe for QOOH intermediates. Moreover, our studies demonstrate that QOOH intermediates undergo absorption at tropospherically relevant near-UV wavelengths, which may contribute to the removal of atmospherically relevant QOOH intermediates derived from the emission of alkenes into the troposphere (e.g., isoprene).

Our studies are also exciting from a physical and theoretical chemistry perspective, as the QOOH intermediates show conformer-dependent changes in the ground-state multi-reference character, as well as the excited-state character. Given these compelling observations, our future studies will focus on the excited-state dynamics of these conformers. Additionally, we will also extend to photochemical studies of ROO and QOOH radicals of increasing molecular complexity—particularly those derived from atmospherically relevant volatile organic compounds. We expect that our studies will motivate experimental physical chemists to carry out experimental measurements of the electronic absorption spectra of experimentally achievable ROO and QOOH.

Supplementary Materials: The following supporting information can be downloaded at: https://www.mdpi.com/article/10.3390/photochem5030026/s1, Figure S1.1: Active space orbitals of ROO; Figure S1.2: Active space orbitals of QOOH-1; Figure S1.3: Active space orbitals of QOOH-2; Figure S1.4: Active space orbitals of QOOH-3 Table S2.1: Normal mode wavenumbers of ROO conformer 1; Table S2.2: Normal mode wavenumbers of ROO conformer 2; Table S2.3: Normal mode wavenumbers of ROO conformer 3; Table S2.4: Normal mode wavenumbers of QOOH conformer 1; Table S2.5: Normal mode wavenumbers of QOOH conformer 2; Table S2.6: Normal mode wavenumbers of QOOH conformer 3.

Author Contributions: Conceptualization, T.N.V.K.; methodology, L.M.G., S.E.G., T.B., B.M. and M.F.V.; formal analysis, L.M.G., B.M., M.F.V. and T.N.V.K.; investigation, L.M.G., S.E.G. and T.B.; resources, T.N.V.K.; data curation, L.M.G., S.E.G. and T.B.; writing—original draft preparation, L.M.G. and T.N.V.K.; writing—review and editing, B.M., M.F.V. and T.N.V.K. All authors have read and agreed to the published version of the manuscript.

Funding: The work is supported by the National Science Foundation (award number 2229695). SEG and TNVK graciously acknowledge the ADVANCE program at UL Lafayette for providing a undergraduate research stipendium for SEG to complete the reported research. This material is based upon work supported by the U.S. Department of Energy, Office of Science, Office of Basic Energy Sciences, under Award Number DE-SC0025691 (MFV).

Data Availability Statement: The underlying data for this is available upon reasonable request to the corresponding authors.

Conflicts of Interest: The authors declare no conflicts of interest.

References

1. Srinivasan, N.K.; Harding, L.B.; Klippenstein, S.J. Experimental and theoretical rate constants for $CH_4 + O_2 \rightarrow CH_3 + HO_2$. *Combust. Flame* **2007**, *149*, 104–111. [CrossRef]
2. Osborn, D.L. Reaction Mechanisms on Multiwell Potential Energy Surfaces in Combustion (and Atmospheric) Chemistry. *Annu. Rev. Phys. Chem.* **2017**, *68*, 233–260. [CrossRef]
3. Zádor, J.; Taatjes, C.A.; Fernandes, R.X. Kinetics of elementary reactions in low-temperature autoignition chemistry. *Prog. Energy Combust. Sci.* **2011**, *37*, 371–421. [CrossRef]
4. Bianchi, F.; Kurtén, T.; Riva, M.; Mohr, C.; Rissanen, M.P.; Roldin, P.; Berndt, T.; Crounse, J.D.; Wennberg, P.O.; Mentel, T.F.; et al. Highly Oxygenated Organic Molecules (HOM) from Gas-Phase Autoxidation Involving Peroxy Radicals: A Key Contributor to Atmospheric Aerosol. *Chem. Rev.* **2019**, *119*, 3472–3509. [CrossRef]
5. Praske, E.; Otkjær, R.V.; Crounse, J.D.; Hethcox, J.C.; Stoltz, B.M.; Kjaergaard, H.G.; Wennberg, P.O. Atmospheric autoxidation is increasingly important in urban and suburban North America. *Proc. Natl. Acad. Sci. USA* **2018**, *115*, 64–69. [CrossRef]
6. Crounse, J.D.; Nielsen, L.B.; Jørgensen, S.; Kjaergaard, H.G.; Wennberg, P.O. Autoxidation of Organic Compounds in the Atmosphere. *J. Phys. Chem. Lett.* **2013**, *4*, 3513–3520. [CrossRef]
7. Wang, Z.; Zhang, L.; Moshammer, K.; Popolan-Vaida, D.M.; Shankar, V.S.B.; Lucassen, A.; Hemken, C.; Taatjes, C.A.; Leone, S.R.; Kohse-Höinghaus, K.; et al. Additional chain-branching pathways in the low-temperature oxidation of branched alkanes. *Combust. Flame* **2016**, *164*, 386–396. [CrossRef]
8. Wang, Z.; Sarathy, S.M. Third O_2 addition reactions promote the low-temperature auto-ignition of n-alkanes. *Combust. Flame* **2016**, *165*, 364–372. [CrossRef]

9. Schervish, M.; Donahue, N.M. Peroxy radical chemistry and the volatility basis set. *Atmos. Chem. Phys.* **2020**, *20*, 1183–1199. [CrossRef]
10. Savee, J.D.; Papajak, E.; Rotavera, B.; Huang, H.; Eskola, A.J.; Welz, O.; Sheps, L.; Taatjes, C.A.; Zádor, J.; Osborn, D.L. Direct observation and kinetics of a hydroperoxyalkyl radical (QOOH). *Science* **2015**, *347*, 643–646. [CrossRef]
11. Ehn, M.; Thornton, J.A.; Kleist, E.; Sipilä, M.; Junninen, H.; Pullinen, I.; Springer, M.; Rubach, F.; Tillmann, R.; Lee, B.; et al. A large source of low-volatility secondary organic aerosol. *Nature* **2014**, *506*, 476–479. [CrossRef] [PubMed]
12. Kalafut-Pettibone, A.J.; Klems, J.P.; Burgess, D.R.; McGivern, W.S. Alkylperoxy Radical Photochemistry in Organic Aerosol Formation Processes. *J. Phys. Chem. A* **2013**, *117*, 14141–14150. [CrossRef]
13. Paulot, F.; Crounse, J.D.; Kjaergaard, H.G.; Kürten, A.; Clair, J.M.S.; Seinfeld, J.H.; Wennberg, P.O. Unexpected Epoxide Formation in the Gas-Phase Photooxidation of Isoprene. *Science* **2009**, *325*, 730–733. [CrossRef] [PubMed]
14. Claeys, M.; Graham, B.; Vas, G.; Wang, W.; Vermeylen, R.; Pashynska, V.; Cafmeyer, J.; Guyon, P.; Andreae, M.O.; Artaxo, P.; et al. Formation of Secondary Organic Aerosols Through Photooxidation of Isoprene. *Science* **2004**, *303*, 1173–1176. [CrossRef]
15. Crounse, J.D.; Paulot, F.; Kjaergaard, H.G.; Wennberg, P.O. Peroxy radical isomerization in the oxidation of isoprene. *Phys. Chem. Chem. Phys.* **2011**, *13*, 13607–13613. [CrossRef] [PubMed]
16. Hallquist, M.; Wenger, J.C.; Baltensperger, U.; Rudich, Y.; Simpson, D.; Claeys, M.; Dommen, J.; Donahue, N.M.; George, C.; Goldstein, A.H.; et al. The formation, properties and impact of secondary organic aerosol: Current and emerging issues. *Atmos. Chem. Phys.* **2009**, *9*, 5155–5236. [CrossRef]
17. Vereecken, L.; Aumont, B.; Barnes, I.; Bozzelli, J.W.; Goldman, M.J.; Green, W.H.; Madronich, S.; Mcgillen, M.R.; Mellouki, A.; Orlando, J.J.; et al. Perspective on Mechanism Development and Structure-Activity Relationships for Gas-Phase Atmospheric Chemistry. *Int. J. Chem. Kinet.* **2018**, *50*, 435–469. [CrossRef]
18. Atkinson, R. Kinetics of the gas-phase reactions of OH radicals with alkanes and cycloalkanes. *Atmos. Chem. Phys.* **2003**, *3*, 2233–2307. [CrossRef]
19. Klems, J.P.; Lippa, K.A.; McGivern, W.S. Quantitative Evidence for Organic Peroxy Radical Photochemistry at 254 nm. *J. Phys. Chem. A* **2015**, *119*, 344–351. [CrossRef]
20. Orlando, J.J.; Tyndall, G.S. Laboratory studies of organic peroxy radical chemistry: An overview with emphasis on recent issues of atmospheric significance. *Chem. Soc. Rev.* **2012**, *41*, 6294–6317. [CrossRef]
21. Boamah, M.D.; Sullivan, K.K.; Shulenberger, K.E.; Soe, C.M.; Jacob, L.M.; Yhee, F.C.; Atkinson, K.E.; Boyer, M.C.; Haines, R.; Arumainayagam, C.R. Low-energy electron-induced chemistry of condensed methanol: Implications for the interstellar synthesis of prebiotic molecules. *Faraday Discuss.* **2014**, *168*, 249–266. [CrossRef]
22. Assaf, E.; Tanaka, S.; Kajii, Y.; Schoemaecker, C.; Fittschen, C. Rate constants of the reaction of C2–C4 peroxy radicals with OH radicals. *Chem. Phys. Lett.* **2017**, *684*, 245–249. [CrossRef]
23. Assaf, E.; Schoemaecker, C.; Vereecken, L.; Fittschen, C. Experimental and theoretical investigation of the reaction of RO_2 radicals with OH radicals: Dependence of the HO_2 yield on the size of the alkyl group. *Int. J. Chem. Kinet.* **2018**, *50*, 670–680. [CrossRef]
24. Biggs, P.; Canosa-Mass, C.E.; Fracheboud, J.-M.; Shallcross, D.E.; Wayne, R.P. Rate constants for the reactions of C_2H_5, C_2H_5O and $C_2H_5O_2$ radicals with NO_3 at 298 K and 2.2 torr. *J. Chem. Soc. Faraday Trans.* **1995**, *91*, 817–825. [CrossRef]
25. Ziemann, P.J.; Atkinson, R. Kinetics, products, and mechanisms of secondary organic aerosol formation. *Chem. Soc. Rev.* **2012**, *41*, 6582–6605. [CrossRef]
26. Eberhard, J.; Howard, C.J. Rate Coefficients for the Reactions of Some C3 to C5 Hydrocarbon Peroxy Radicals with NO. *J. Phys. Chem. A* **1997**, *101*, 3360–3366. [CrossRef]
27. Peng, Z.; Jimenez, J.L. Radical chemistry in oxidation flow reactors for atmospheric chemistry research. *Chem. Soc. Rev.* **2020**, *49*, 2570–2616. [CrossRef] [PubMed]
28. Jenkin, M.E.; Valorso, R.; Aumont, B.; Rickard, A.R. Estimation of rate coefficients and branching ratios for reactions of organic peroxy radicals for use in automated mechanism construction. *Atmos. Chem. Phys.* **2019**, *19*, 7691–7717. [CrossRef]
29. Berndt, T.; Scholz, W.; Mentler, B.; Fischer, L.; Herrmann, H.; Kulmala, M.; Hansel, A. Accretion Product Formation from Self- and Cross-Reactions of RO_2 Radicals in the Atmosphere. *Angew. Chem. Int. Ed.* **2018**, *57*, 3820–3824. [CrossRef] [PubMed]
30. Archibald, A.T.; Petit, A.S.; Percival, C.J.; Harvey, J.N.; Shallcross, D.E. On the importance of the reaction between OH and RO_2 radicals. *Atmos. Sci. Lett.* **2009**, *10*, 102–108. [CrossRef]
31. Chen, L.W.; Hung, C.M.; Matsui, H.; Lee, Y.P. New experimental evidence to support roaming in the reaction Cl^+ isobutene (i-C4 H8). *Sci. Rep.* **2017**, *7*, 40105.
32. Yan, C.; Kocevska, S.; Krasnoperov, L.N. Kinetics of the Reaction of CH3O2 Radicals with OH Studied over the 292–526 K Temperature Range. *J. Phys. Chem. A* **2016**, *120*, 6111–6121. [CrossRef]
33. Assaf, E.; Sheps, L.; Whalley, L.; Heard, D.; Tomas, A.; Schoemaecker, C.; Fittschen, C. The Reaction between CH_3O_2 and OH Radicals: Product Yields and Atmospheric Implications. *Environ. Sci. Technol.* **2017**, *51*, 2170–2177. [CrossRef] [PubMed]

34. Boyd, A.A.; Villenave, E.; Lesclaux, R. Structure–reactivity relationships for the self- reactions of linear secondary alkylperoxy radicals: An experimental investigation. *Int. J. Chem. Kinet.* **1999**, *31*, 37–46. [CrossRef]
35. Eberhard, J.; Howard, C.J. Temperature-dependent kinetics studies of the reactions of $C_2H_5O_2$ and n-$C_3H_7O_2$ radicals with NO. *Int. J. Chem. Kinet.* **1996**, *28*, 731–740. [CrossRef]
36. Faragó, E.P.; Schoemaecker, C.; Viskolcz, B.; Fittschen, C. Experimental determination of the rate constant of the reaction between $C_2H_5O_2$ and OH radicals. *Chem. Phys. Lett.* **2015**, *619*, 196–200. [CrossRef]
37. Jokinen, T.; Sipilä, M.; Richters, S.; Kerminen, V.-M.; Paasonen, P.; Stratmann, F.; Worsnop, D.; Kulmala, M.; Ehn, M.; Herrmann, H.; et al. Rapid autoxidation forms highly oxidized RO_2 radicals in the atmosphere. *Angew. Chem. Int. Ed. Engl.* **2014**, *53*, 14596–14600. [CrossRef] [PubMed]
38. Lightfoot, P.D.; Cox, R.A.; Crowley, J.N.; Destriau, M.; Hayman, G.D.; Jenkin, M.E.; Moortgat, G.K.; Zabel, F. Organic peroxy radicals: Kinetics, spectroscopy and tropospheric chemistry. *Atmos. Environ. Part A General. Top.* **1992**, *26*, 1805–1961. [CrossRef]
39. Pilling, M.J. Basic chemistry of combustion. In *Low-Temperature Combustion and Autoignition*; Elsevier: Amsterdam, The Netherlands, 1997.
40. Kaiser, E.W. Temperature and Pressure Dependence of the C_2H_4 Yield from the Reaction C_2H_5 + O_2. *J. Phys. Chem.* **1995**, *99*, 707–711. [CrossRef]
41. Kaiser, E.W. Formation of C_3H_6 from the Reaction C_3H_7 + O_2 between 450 and 550 K. *J. Phys. Chem. A* **1998**, *102*, 5903–5906. [CrossRef]
42. Kaiser, E.W.; Wallington, T.J. Formation of C3H6 from the Reaction C_3H_7 + O_2 and $C_2H_3C_l$ from $C_2H_4C_l$ + O_2 at 297 K. *J. Phys. Chem.* **1996**, *100*, 18770–18774. [CrossRef]
43. Plumb, I.C.; Ryan, K.R. Kinetic studies of the reaction of C_2H_5 with O_2 at 295 K. *Int. J. Chem. Kinet.* **1981**, *13*, 1011–1028. [CrossRef]
44. Sharma, S.; Raman, S.; Green, W.H. Intramolecular Hydrogen Migration in Alkylperoxy and Hydroperoxyalkylperoxy Radicals: Accurate Treatment of Hindered Rotors. *J. Phys. Chem. A* **2010**, *114*, 5689–5701. [CrossRef]
45. DeSain, J.D.; Taatjes, C.A. Infrared Frequency-Modulation Probing of Product Formation in Alkyl + O_2 Reactions: III. The Reaction of Cyclopentyl Radical (c-C_5H_9) with O_2 between 296 and 723 K. *J. Phys. Chem. A* **2001**, *105*, 6646–6654. [CrossRef]
46. Clifford, E.P.; Farrell, J.T.; DeSain, J.D.; Taatjes, C.A. Infrared Frequency-Modulation Probing of Product Formation in Alkyl + O_2 Reactions: I. The Reaction of C_2H_5 with O_2 between 295 and 698 K. *J. Phys. Chem. A* **2000**, *104*, 11549–11560. [CrossRef]
47. DeSain, J.D.; Clifford, E.P.; Taatjes, C.A. Infrared Frequency-Modulation Probing of Product Formation in Alkyl + O_2 Reactions: II. The Reaction of C_3H_7 with O_2 between 296 and 683 K. *J. Phys. Chem. A* **2001**, *105*, 3205–3213. [CrossRef]
48. DeSain, J.D.; Taatjes, C.A.; Miller, J.A.; Klippenstein, S.J.; Hahn, D.K. Infrared frequency-modulation probing of product formation in alkyl + O_2 reactions. Part IV. Reactions of propyl and butyl radicals with O_2. *Faraday Discuss.* **2002**, *119*, 101–120. [CrossRef]
49. Kaiser, E.W.; Lorkovic, I.M.; Wallington, T.J. Pressure dependence of the ethene yield from the reaction ethyl radical + oxygen. *J. Phys. Chem.* **1990**, *94*, 3352–3354. [CrossRef]
50. Estupiñán, E.G.; Smith, J.D.; Tezaki, A.; Klippenstein, S.J.; Taatjes, C.A. Measurements and Modeling of DO_2 Formation in the Reactions of C_2D_5 and C_3D_7 Radicals with O_2. *J. Phys. Chem. A* **2007**, *111*, 4015–4030. [CrossRef] [PubMed]
51. Westbrook, C.K. Chemical kinetics of hydrocarbon ignition in practical combustion systems. *Proc. Combust. Inst.* **2000**, *28*, 1563–1577. [CrossRef]
52. Miller, J.A.; Klippenstein, S.J.; Robertson, S.H. A theoretical analysis of the reaction between ethyl and molecular oxygen. *Proc. Combust. Inst.* **2000**, *28*, 1479–1486. [CrossRef]
53. Rienstra-Kiracofe, J.C.; Allen, W.D.; Schaefer, H. The C_2H_5 + O_2 Reaction Mechanism: High-Level ab Initio Characterizations. *J. Phys. Chem. A* **2000**, *104*, 9823–9840. [CrossRef]
54. Estupiñán, E.G.; Klippenstein, S.J.; Taatjes, C.A. Measurements and Modeling of HO_2 Formation in the Reactions of n-C_3H_7 and i-C_3H_7 Radicals with O_2. *J. Phys. Chem. B* **2005**, *109*, 8374–8387. [CrossRef]
55. Kaiser, E.W. Mechanism of the Reaction C_2H_5 + O_2 from 298 To 680 K. *J. Phys. Chem. A* **2002**, *106*, 1256–1265. [CrossRef]
56. DeSain, J.D.; Klippenstein, S.J.; Miller, J.A.; Taatjes, C.A. Measurements, Theory, and Modeling of OH Formation in Ethyl + O_2 and Propyl + O_2 Reactions. *J. Phys. Chem. A* **2003**, *107*, 4415–4427. [CrossRef]
57. Sheng, C.Y.; Bozzelli, J.W.; Dean, A.M.; Chang, A.Y. Detailed Kinetics and Thermochemistry of C_2H_5 + O_2: Reaction Kinetics of the Chemically-Activated and Stabilized CH_3CH_2OO• Adduct. *J. Phys. Chem. A* **2002**, *106*, 7276–7293. [CrossRef]
58. Quelch, G.E.; Gallo, M.M.; Schaefer, H.F. Aspects of the reaction mechanism of ethane combustion. Conformations of the ethylperoxy radical. *J. Am. Chem. Soc.* **1992**, *114*, 8239–8247. [CrossRef]
59. Quelch, G.E.; Gallo, M.M.; Shen, M.; Xie, Y.; Schaefer, H.F.; Moncrieff, D. Aspects of the Reaction Mechanism of Ethane Combustion. 2. Nature of the Intramolecular Hydrogen Transfer. *J. Am. Chem. Soc.* **1994**, *116*, 4953–4962. [CrossRef]
60. Miller, J.A.; Klippenstein, S.J. The reaction between ethyl and molecular oxygen II: Further analysis. *Int. J. Chem. Kinet.* **2001**, *33*, 654–668. [CrossRef]
61. Chen, C.-J.; Bozzelli, J.W. Analysis of Tertiary Butyl Radical + O_2, Isobutene + HO_2, Isobutene + OH, and Isobutene−OH Adducts + O_2: A Detailed Tertiary Butyl Oxidation Mechanism. *J. Phys. Chem. A* **1999**, *103*, 9731–9769. [CrossRef]

62. DeSain, J.D.; Klippenstein, S.J.; Taatjes, C.A. Time-resolved measurements of OH and HO2 product formation in pulsed-photolytic chlorine atom initiated oxidation of neopentane. *Phys. Chem. Chem. Phys.* **2003**, *5*, 1584–1592. [CrossRef]
63. Petway, S.V.; Ismail, H.; Green, W.H.; Estupiñán, E.G.; Jusinski, L.E.; Taatjes, C.A. Measurements and Automated Mechanism Generation Modeling of OH Production in Photolytically Initiated Oxidation of the Neopentyl Radical. *J. Phys. Chem. A* **2007**, *111*, 3891–3900. [CrossRef]
64. Sun, H.; Bozzelli, J.W. Thermochemical and Kinetic Analysis on the Reactions of Neopentyl and Hydroperoxy-Neopentyl Radicals with Oxygen: Part I. OH and Initial Stable HC Product Formation. *J. Phys. Chem. A* **2004**, *108*, 1694–1711. [CrossRef]
65. Curran, H.J.; Gaffuri, P.; Pitz, W.J.; Westbrook, C.K. A Comprehensive Modeling Study of n-Heptane Oxidation. *Combust. Flame* **1998**, *114*, 149–177. [CrossRef]
66. Curran, H.J.; Gaffuri, P.; Pitz, W.J.; Westbrook, C.K. A comprehensive modeling study of iso-octane oxidation. *Combust. Flame* **2002**, *129*, 253–280. [CrossRef]
67. Zhu, L.; Bozzelli, J.W.; Kardos, L.M. Thermochemical Properties, ΔfH°(298), S°(298), and Cp°(T), for n-Butyl and n-Pentyl Hydroperoxides and the Alkyl and Peroxy Radicals, Transition States, and Kinetics for Intramolecular Hydrogen Shift Reactions of the Peroxy Radicals. *J. Phys. Chem. A* **2007**, *111*, 6361–6377. [CrossRef] [PubMed]
68. Merle, J.K.; Hayes, C.J.; Zalyubovsky, S.J.; Glover, B.G.; Miller, T.A.; Hadad, C.M. Theoretical Determinations of the Ambient Conformational Distribution and Unimolecular Decomposition of n-Propylperoxy Radical. *J. Phys. Chem. A* **2005**, *109*, 3637–3646. [CrossRef] [PubMed]
69. Sirjean, B.; Glaude, P.A.; Ruiz-Lòpez, M.F.; Fournet, R. Theoretical kinetic study of the reactions of cycloalkylperoxy radicals. *J. Phys. Chem. A* **2009**, *113*, 6924–6935. [CrossRef]
70. Silke, E.J.; Pitz, W.J.; Westbrook, C.K.; Ribaucour, M. Detailed Chemical Kinetic Modeling of Cyclohexane Oxidation†. *J. Phys. Chem. A* **2007**, *111*, 3761–3775. [CrossRef]
71. Knepp, A.M.; Meloni, G.; Jusinski, L.E.; Taatjes, C.A.; Cavallotti, C.; Klippenstein, S.J. Theory, measurements, and modeling of OH and HO_2 formation in the reaction of cyclohexyl radicals with O_2. *Phys. Chem. Chem. Phys.* **2007**, *9*, 4315–4331. [CrossRef]
72. Whelan, C.A.; Blitz, M.A.; Shannon, R.; Onel, L.; Lockhart, J.P.; Seakins, P.W.; Stone, D. Temperature and Pressure Dependent Kinetics of QOOH Decomposition and Reaction with O2: Experimental and Theoretical Investigations of QOOH Radicals Derived from Cl + $(CH_3)_3$COOH. *J. Phys. Chem. A* **2019**, *123*, 10254–10262. [CrossRef]
73. Zádor, J.; Huang, H.; Welz, O.; Zetterberg, J.; Osborn, D.L.; Taatjes, C.A. Directly measuring reaction kinetics of ˙QOOH—A crucial but elusive intermediate in hydrocarbon autoignition. *Phys. Chem. Chem. Phys.* **2013**, *15*, 10753–10760. [CrossRef]
74. Bugler, J.; Power, J.; Curran, H.J. A theoretical study of cyclic ether formation reactions. *Proc. Combust. Inst.* **2017**, *36*, 161–167. [CrossRef]
75. Bhagde, T.; Hansen, A.S.; Chen, S.; Walsh, P.J.; Klippenstein, S.J.; Lester, M.I. Energy-resolved and time-dependent unimolecular dissociation of hydroperoxyalkyl radicals (˙QOOH). *Faraday Discuss.* **2022**, *238*, 575–588. [CrossRef]
76. Hansen, A.S.; Bhagde, T.; Moore, K.B.; Moberg, D.R.; Jasper, A.W.; Georgievskii, Y.; Vansco, M.F.; Klippenstein, S.J.; Lester, M.I. Watching a hydroperoxyalkyl radical (•QOOH) dissociate. *Science* **2021**, *373*, 679–682. [CrossRef] [PubMed]
77. Qian, Y.; Roy, T.K.; Jasper, A.W.; Sojdak, C.A.; Kozlowski, M.C.; Klippenstein, S.J.; Lester, M.I. Isomer-resolved unimolecular dynamics of the hydroperoxyalkyl intermediate (•QOOH) in cyclohexane oxidation. *Proc. Natl. Acad. Sci. USA* **2024**, *121*, e2401148121. [CrossRef] [PubMed]
78. Roy, T.K.; Qian, Y.; Sojdak, C.A.; Kozlowski, M.C.; Klippenstein, S.J.; Lester, M.I. Infrared signature of the hydroperoxyalkyl intermediate (•QOOH) in cyclohexane oxidation: An isomer-resolved spectroscopic study. *J. Chem. Phys.* **2024**, *161*, 034302. [CrossRef] [PubMed]
79. Qian, Y.; Roy, T.K.; Valente, D.S.; Cruz, E.M.; Kozlowski, M.C.; Della Libera, A.; Klippenstein, S.J.; Lester, M.I. Infrared Fingerprint and Unimolecular Decay Dynamics of the Hydroperoxyalkyl Intermediate (•QOOH) in Cyclopentane Oxidation. *J. Phys. Chem. A* **2024**, *128*, 9240–9250. [CrossRef]
80. Wallington, T.J.; Dagaut, P.; Kurylo, M.J. UV absorption cross sections and reaction kinetics and mechanisms for peroxy radicals in the gas phase. *Chem. Rev.* **1992**, *92*, 667–710. [CrossRef]
81. Glover, B.G.; Miller, T.A. Near-IR Cavity Ringdown Spectroscopy and Kinetics of the Isomers and Conformers of the Butyl Peroxy Radical. *J. Phys. Chem. A* **2005**, *109*, 11191–11197. [CrossRef]
82. Frost, G.J.; Ellison, G.B.; Vaida, V. Organic Peroxyl Radical Photolysis in the Near-Infrared: Effects on Tropospheric Chemistry. *J. Phys. Chem. A* **1999**, *103*, 10169–10178. [CrossRef]
83. Zhang, C.; Shamas, M.; Assali, M.; Tang, X.; Zhang, W.; Pillier, L.; Schoemaecker, C.; Fittschen, C. Absolute Absorption Cross-Section of the Ã←X Electronic Transition of the Ethyl Peroxy Radical and Rate Constant of Its Cross Reaction with HO_2. *Photonics* **2021**, *8*, 296. [CrossRef]
84. Atkinson, D.B.; Spillman, J.L. Alkyl Peroxy Radical Kinetics Measured Using Near-infrared CW−Cavity Ring-down Spectroscopy. *J. Phys. Chem. A* **2002**, *106*, 8891–8902. [CrossRef]

85. Melnik, D.; Chhantyal-Pun, R.; Miller, T.A. Measurements of the Absolute Absorption Cross Sections of the Ã←X Transition in Organic Peroxy Radicals by Dual-Wavelength Cavity Ring-Down Spectroscopy. *J. Phys. Chem. A* **2010**, *114*, 11583–11594. [CrossRef] [PubMed]
86. Pushkarsky, M.B.; Zalyubovsky, S.J.; Miller, T.A. Detection and characterization of alkyl peroxy radicals using cavity ringdown spectroscopy. *J. Chem. Phys.* **2000**, *112*, 10695–10698. [CrossRef]
87. Nichols, B.; Sullivan, E.N.; Ryazanov, M.; Hong, C.M.; Neumark, D.M. Investigation of the two- and three-fragment photodissociation of the tert-butyl peroxy radical at 248 nm. *J. Chem. Phys.* **2017**, *147*, 134304. [CrossRef]
88. Franke, P.R.; Moore, K.B.; Schaefer, H.F.; Douberly, G.E. tert-Butyl peroxy radical: Ground and first excited state energetics and fundamental frequencies. *Phys. Chem. Chem. Phys.* **2019**, *21*, 9747–9758. [CrossRef] [PubMed]
89. Copan, A.V.; Schaefer III, H.F.; Agarwal, J. Examining the ground and first excited states of methyl peroxy radical with high-level coupled-cluster theory. *Mol. Phys.* **2015**, *113*, 2992–2998. [CrossRef]
90. Vansco, M.F.; Zuraski, K.; Winiberg, F.A.F.; Au, K.; Trongsiriwat, N.; Walsh, P.J.; Osborn, D.L.; Percival, C.J.; Klippenstein, S.J.; Taatjes, C.A.; et al. Functionalized hydroperoxide formation from the reaction of methacrolein-oxide, an isoprene-derived criegee intermediate, with formic acid: Experiment and theory. *Molecules* **2021**, *26*, 3058. [CrossRef]
91. Poirier, C.A.; Guidry, L.M.; Ratliff, J.M.; Esposito, V.J.; Marchetti, B.; Karsili, T.N.V. Modeling the Ground- and Excited-State Unimolecular Decay of the Simplest Fluorinated Criegee Intermediate, HFCOO, Formed from the Ozonolysis of Hydrofluoroolefin Refrigerants. *J. Phys. Chem. A* **2023**, *127*, 6377–6384. [CrossRef]
92. Guidry, L.M.; Bardash, L.A.; Yigiter, A.; Ravi, S.; Marchetti, B.; Karsili, T.N.V. The role of solar photolysis in the atmospheric removal of methacrolein oxide and the methacrolein oxide—Water van-der Waals complex in pristine environments. *Photochem. Photobiol.* **2024**, *101*, 423–433. [CrossRef]
93. Vansco, M.F.; Caravan, R.L.; Zuraski, K.; Winiberg, F.A.F.; Au, K.; Trongsiriwat, N.; Walsh, P.J.; Osborn, D.L.; Percival, C.J.; Khan, M.A.H.; et al. Experimental Evidence of Dioxole Unimolecular Decay Pathway for Isoprene-Derived Criegee Intermediates. *J. Phys. Chem. A* **2020**, *124*, 3542–3554. [CrossRef]
94. Roy, T.K.; Qian, Y.; Karlsson, E.; Rabayah, R.; Sojdak, C.A.; Kozlowski, M.C.; Karsili, T.N.V.; Lester, M.I. Vibrational spectroscopy and dissociation dynamics of cyclohexyl hydroperoxide. *Chem. Sci.* **2024**, *15*, 6160–6167. [CrossRef]
95. Werner, H.J.; Knowles, P.J.; Knizia, G.; Manby, F.R.; Schütz, M. Molpro: A general-purpose quantum chemistry program package. *Wiley Interdiscip. Rev. Comput. Mol. Sci.* **2012**, *2*, 242–253. [CrossRef]
96. Werner, H.-J.; Knowles, P.J.; Knizia, G.; Manby, F.R.; Schütz, M.; Celani, P.; Györffy, W.; Kats, D.; Korona, T.; Lindh, R.; et al. *MOLPRO*, Version 2018.1; a Package of ab Initio Programs; Institute for Theoretical Chemistry, University of Stuttgart: Stuttgart, Germany, 2018.
97. Frisch, D.J.F.M.J.; Trucks, G.W.; Schlegel, H.B.; Scuseria, G.E.; Robb, M.A.; Cheeseman, J.R.; Scalmani, G.; Barone, V.; Petersson, G.A.; Nakatsuji, H.; et al. *Gaussian 16*, Revision C.01; Gaussian Inc.: Wallingford, CT, USA, 2016.
98. McCoy, J.C.; Marchetti, B.; Thodika, M.; Karsili, T.N.V. A Simple and Efficient Method for Simulating the Electronic Absorption Spectra of Criegee Intermediates: Benchmarking on CH_2OO and CH_3CHOO. *J. Phys. Chem. A* **2021**, *125*, 4089–4097. [CrossRef]
99. McCoy, J.C.; Léger, S.J.; Frey, C.F.; Vansco, M.F.; Marchetti, B.; Karsili, T.N.V.; Marchetti, B.; Karsili, T.N.V. Modeling the Conformer-Dependent Electronic Absorption Spectra and Photolysis Rates of Methyl Vinyl Ketone Oxide and Methacrolein Oxide. *J. Phys. Chem. A* **2022**, *126*, 485–496. [CrossRef]
100. Wang, G.; Liu, T.; Zou, M.; Sojdak, C.A.; Kozlowski, M.C.; Karsili, T.N.; Lester, M.I. Electronic Spectroscopy and Dissociation Dynamics of Vinyl-Substituted Criegee Intermediates: 2-Butenal Oxide and Comparison with Methyl Vinyl Ketone Oxide and Methacrolein Oxide Isomers. *J. Phys. Chem. A* **2022**, *127*, 203–215. [CrossRef] [PubMed]
101. Karlsson, E.; Rabayah, R.; Liu, T.; Cruz, E.M.; Kozlowski, M.C.; Karsili, T.N.V.; Lester, M.I. Electronic Spectroscopy of the Halogenated Criegee Intermediate, ClCHOO: Experiment and Theory. *J. Phys. Chem. A* **2024**, *128*, 10949–10956. [CrossRef] [PubMed]
102. Prlj, A.; Hollas, D.; Curchod, B.F.E. Deciphering the Influence of Ground-State Distributions on the Calculation of Photolysis Observables. *J. Phys. Chem. A* **2023**, *127*, 7400–7409. [CrossRef] [PubMed]
103. Hansen, A.S.; Bhagde, T.; Qian, Y.; Cavazos, A.; Huchmala, R.M.; Boyer, M.A.; Gavin-Hanner, C.F.; Klippenstein, S.J.; McCoy, A.B.; Lester, M.I. Infrared spectroscopic signature of a hydroperoxyalkyl radical (•QOOH). *J. Chem. Phys.* **2021**, *156*, 14301. [CrossRef]
104. Beames, J.M.; Liu, F.; Lu, L.; Lester, M.I. UV spectroscopic characterization of an alkyl substituted Criegee intermediate CH_3CHOO. *J. Chem. Phys.* **2013**, *138*, 244307. [CrossRef] [PubMed]
105. Li, H.; Fang, Y.; Beames, J.M.; Lester, M.I. Velocity map imaging of O-atom products from UV photodissociation of the CH_2OO Criegee intermediate. *J. Chem. Phys.* **2015**, *142*, 214312. [CrossRef]
106. Wang, G.; Liu, T.; Zou, M.; Karsili, T.N.V.; Lester, M.I. UV photodissociation dynamics of the acetone oxide Criegee intermediate: Experiment and theory. *Phys. Chem. Chem. Phys.* **2023**, *25*, 7453–7465. [CrossRef]

107. Esposito, V.J.; Liu, T.; Wang, G.; Caracciolo, A.; Vansco, M.F.; Marchetti, B.; Karsili, T.N.V.; Lester, M.I. Photodissociation Dynamics of CH_2OO on Multiple Potential Energy Surfaces: Experiment and Theory. *J. Phys. Chem. A* **2021**, *125*, 6571–6579. [CrossRef] [PubMed]
108. Wang, G.; Liu, T.; Caracciolo, A.; Vansco, M.F.; Trongsiriwat, N.; Walsh, P.J.; Marchetti, B.; Karsili, T.N.V.; Lester, M.I. Photodissociation dynamics of methyl vinyl ketone oxide: A four-carbon unsaturated Criegee intermediate from isoprene ozonolysis. *J. Chem. Phys.* **2021**, *155*, 174305. [CrossRef] [PubMed]